

Article

Radiation Effects in Amorphous Metallic Alloys as Revealed by Mössbauer Spectrometry: Part I. Neutron Irradiation

Marcel B. Miglierini ^{1,2} 

¹ Institute of Nuclear and Physical Engineering, Faculty of Electrical Engineering and Information Technology, Slovak University of Technology in Bratislava, Ilkovičova 3, 812 19 Bratislava, Slovakia; marcel.miglierini@stuba.sk

² Department of Nuclear Reactors, Faculty of Nuclear Sciences and Physical Engineering, Czech Technical University, V Holešovičkách 2, 180 00 Prague, Czech Republic

Abstract: Iron-based amorphous metallic alloys (AMAs) of several compositions were exposed to neutron irradiation with fluences of up to 10^{19} n/cm². These materials exhibit excellent magnetic properties which predetermine them for use in electronic devices operated also in radiation-exposed environments. Response of the studied AMAs to neutron irradiation is followed by Mössbauer spectrometry which probes the local microstructure. Neutron irradiation leads to rearrangement of constituent atoms, their clustering, and formation of stress centers. The observed modifications of topological short-range order result in changes of spectral parameters including average hyperfine magnetic field, $\langle B \rangle$, standard deviation of the distribution of hyperfine fields, and position of the net magnetic moment. After irradiation, especially differences in $\langle B \rangle$ -values develop in two opposite directions. This apparent controversy can be explained by formation of specific atomic pairs with different exchange interactions, which depend on the composition of the samples. Part II of this paper will be devoted to radiation effects caused in Fe-based AMAs by ion irradiation.



Citation: Miglierini, M.B. Radiation Effects in Amorphous Metallic Alloys as Revealed by Mössbauer Spectrometry: Part I. Neutron Irradiation. *Metals* **2021**, *11*, 845. <https://doi.org/10.3390/met11050845>

Academic Editor: Alexander V. Shelyakov

Received: 16 April 2021
Accepted: 18 May 2021
Published: 20 May 2021

Publisher's Note: MDPI stays neutral with regard to jurisdictional claims in published maps and institutional affiliations.



Copyright: © 2021 by the author. Licensee MDPI, Basel, Switzerland. This article is an open access article distributed under the terms and conditions of the Creative Commons Attribution (CC BY) license (<https://creativecommons.org/licenses/by/4.0/>).

Keywords: Mössbauer spectrometry; amorphous metallic alloys; structural modifications; neutron irradiation; hyperfine interactions; short-range order

1. Introduction

New demands of the market as well as developing ecological attitudes of the society require the use of advanced materials [1]. Along with (poly)crystalline steels, other types of metallic materials, namely amorphous metallic alloys (AMAs), are widely used also in industry. They feature disordered structure and that is why they are also referred to as metallic glasses (MGs) and these two terms are used as synonyms. Especially iron-based AMAs exhibit excellent magnetic properties [2,3], which result in a number of applications (e.g., magnetic shielding, transformers cores, and magnetic sensors) [4,5]. Combination of enhanced corrosion resistance and high neutron absorption capacity makes namely chromium- and boron-containing AMAs [6] perspective materials for the use in the nuclear power industry. Possible applications comprise surface coatings of storage containers for spent nuclear fuel [7]. Selected AMAs are considered for construction of magnetic cores of accelerator radio frequency cavities [8] due to advantageous magnetic performance. In this particular application, they could be exposed to lost primary ions and/or subsequently formed neutrons. Accordingly, they are considered as appropriate materials in radiation-exposed environments. Microstructure of materials is sensitive to any external modification which, consequently, affects also their resulting physical properties. The long-term reliability of structural nuclear materials operating under harsh conditions of intense radiation, high temperature and in the presence of corrosion agents is an important technologic, economic and environmental demand, and it raises a number of challenges [9]. Recently their use in remediation of copper contaminated soil [10] and biomedical applications [11] were reported.

Considerable worldwide research effort is dedicated to the design, production, and prediction of resulting properties of new materials that are supposed to be used in extreme environments including harsh conditions of enhanced radiation. Among them, AMAs constitute an interesting class of perspective materials. Though they were invented several decades ago, their structure-to-properties relationship is still not fully understood. Question of their structural arrangement and transformations are solved by the help of atomistic simulations [12]. Continuing experimental effort to describe their unique physical properties is demonstrated by the most recent studies. Along with well-known compositions [13–15], also novel types of AMAs [16,17] are studied with the aim to describe microstructural arrangement and its impact upon the resulting physical properties. In addition, structural transformations into nanocrystalline alloys featuring nanoglass and nanocrystalline regions after heating and deformation were recently reviewed [18].

Knowledge of microstructural arrangement of any materials is crucial as it affects the resulting macroscopic properties. Especially if local structural variations caused by irradiation are considered. Consequently, due attention is paid to the radiation damage which might affect the performance even of such materials, as, for example, steels that are used for construction of reactor pressure vessels [19]. However, unlike the well-defined long-range order in crystalline materials, the atomic arrangement in disordered AMAs is still not sufficiently understood. Thus, their characterization at the atomic level represents an ambitious mission requiring application of advanced experimental techniques. Responses of namely Fe-based AMAs to various kinds of irradiation are widely examined. Examples of such studies include irradiation with gamma photons [20], lasers [21], electron beams with low [22] and high [23] doses, light [24] and heavy [25] ions as well as neutrons which are treated to more details in this work. Consequently, it is inevitable to study the impact of neutron irradiation on their structural as well as magnetic characteristics.

Originally, it was expected that AMAs should be unaffected by radiation damage due to their homogeneous disordered structure, which should accommodate the induced defects. Indeed, as reported by Violet et al. [26], the effects of neutron irradiation on magnetic properties of Fe-Ni-Zr were small, suggesting a good resistance against radiation damage up to fluences of 10^{17} n/cm². It should be noted; however, that the irradiation was performed with 14 MeV neutrons obtained from a neutron generator (i.e., fast neutrons which penetrate relatively easily through thin AMAs ribbons). Nevertheless, the results obtained during the last three decades pointed out that irradiation by neutrons not only results in post irradiation activity [27], but can induce changes in microstructure of AMAs, with a consequent impact upon their magnetic [28–35] and mechanical properties [36,37].

Modification of magnetic parameters of AMAs caused by neutron irradiation represents an important concern of the research groups. A relatively large value of high-field susceptibility of a neutron-irradiated Fe₇₄Ni₂₅B₁₈Si₁₀ AMA was ascribed to inhomogeneities introduced in the amorphous structure, which also caused a decrease in ac susceptibility and an increase in coercivity [29]. These studies were conducted by conventional magnetic measurements using induction magnetometer and AC bridge of mutual inductance. The obtained results were in agreement with the conclusions derived from ferromagnetic resonance experiments performed upon the same samples [30]. A decrease in the value of exchange constant after neutron irradiation of Fe₈₀B₂₀ amorphous ribbons was attributed to atomic rearrangements towards disordering [31]. The same mechanism was thought to cause a decrease of Curie temperature and the spin-wave stiffness constant in neutron-irradiated Fe₃₀Ni_{48-x}Cr_xMo₂Si₅B₁₅ ($x = 4, 10, 12$) MG [32]. Possible irradiation-induced effects of structural and chemical changes in the investigated AMAs were suggested. Nevertheless, the findings obtained from (macroscopic) magnetic measurements by temperature dependencies of spontaneous magnetization and low-field AC susceptibility were not able to unveil subtle structural modifications that took place on an atomic level. These can be effectively revealed by Mössbauer spectrometry.

Another important consequence of neutron irradiation concerns mechanical properties of AMAs exposed to radiation damage. They behave differently from crystalline

alloys, where irradiation-caused embrittlement was found. Some AMAs became even more ductile after neutron irradiation [36]. Majority of the irradiation-induced defect structure was; however, eventually recovered after suitable prolonged heat treatment at temperatures well below the onset of crystallization [37]. In the so-called nanocrystalline alloys (NCAs), which are prepared by appropriately controlled crystallization of AMAs featuring specific composition and consist of amorphous and (nano)crystalline regions [38], neutron irradiation had a different impact upon both types of structures. While thermally embrittled amorphous samples were able to regain complete ductility after neutron irradiation, their nanocrystalline counterparts have shown the same level of brittleness as before the irradiation [39,40]. On the other hand, neutron irradiation of NCAs has led to partial re-amorphization. In both states of the investigated samples (i.e., amorphous and nanocrystalline), deterioration of their magnetic properties occurred after irradiation with sufficiently high neutron fluences of about 10^{18} – 10^{19} n/cm². The observed changes were less significant in the nanocrystalline samples [39,40].

Determination of structural arrangement and hyperfine interactions between the nucleus and the electron shell of iron atoms can be readily obtained by means of ⁵⁷Fe Mössbauer spectrometry. Because iron is the basic constituent element of a broad family of AMAs, namely these systems are especially suited for detailed characterization by this technique, which provides simultaneous information on short-range order (SRO) and magnetic microstructure. It also gives distributions of particular hyperfine parameters. Indeed, the first Mössbauer spectrometry investigations of neutron-irradiated AMAs [41,42] appeared soon after the impact of neutrons on their magnetic properties was reported [29,30].

As it turned out later [43–46], it can be effectively used in the investigation of neutron-irradiated MGs. At the same time, Mössbauer spectrometry is a powerful analytical tool also for characterization of NCAs where several structurally different regions exist, which can be readily identified from the recorded spectra [47,48]. That is why it is not surprising that this technique was successfully applied to investigations of neutron-irradiation-induced modifications of several types of NCAs [49–54] too. The author's contribution to the field of neutron-irradiated AMAs can be found elsewhere [55–61].

In fact, there are not too many experimental studies devoted to the investigation of the effect of neutron irradiation on AMAs. We can only speculate that it is due to technical and safety restrictions associated with the necessity to employ a rather intensive source of neutrons (usually nuclear reactor) and manipulation with radioactive specimens, respectively. Nevertheless, interest in this topic has increased lately, as documented by recently published papers. As examples, the works of Yang et al. [62] and Brechtel et al. [63] can be mentioned. A series of experimental measurements and theoretical simulations were applied to unveil structural responses of ZrCu metallic glass to neutron irradiation [62]. Multiple mechanical property and structural characterization techniques revealed that irradiation of bulk metallic glass $Zr_{52.5}Cu_{17.9}Ni_{14.6}Al_{10}Ti_5$ with neutrons to a fluence of 1.4×10^{20} n/cm² has led to softening and reduced Young's modulus, while opposite effects were found after annealing at 300–325 °C [63]. A new trend in this field makes use of numerical calculations to assess microstructural evolution of MGs under neutron irradiation [64]. However, the wider use of Mössbauer spectrometry in this area of research still does not sufficiently match its potential.

The main purpose of this study rests with identification of microstructural modifications caused by neutron irradiation in Fe-based AMAs prepared by rapid quenching method. Its task is to demonstrate radiation effects using selected examples of AMAs with different chemical compositions. Because they exhibit suitable magnetic parameters, influence of neutron irradiation upon variations of hyperfine interactions will be highlighted too. In doing so, results obtained by employing ⁵⁷Fe Mössbauer spectrometry are reviewed with emphasis on own investigations. It should be noted that nanocrystalline alloys, which are often prepared from AMAs' precursors by suitable heat treatment, are beyond the scope of the present communication and that is why they are mentioned only briefly. Extension

of this work towards radiation effects in AMAs caused by ion irradiation will follow in Part II of this work.

2. Materials and Methods

2.1. Mössbauer Spectrometry

An effective way of microstructural analysis, which becomes especially important when we are interested in radiation damage, is possible through subtle changes in the positions of the nuclear energetic levels. Nuclei of ^{57}Fe in the investigated material are exposed to electric and magnetic fields created by the electrons of the atom itself and by other atoms in its neighborhood. These fields generally interact with the electric charge distribution and the magnetic dipole moment of the nucleus and perturb its nuclear energy states. This perturbation, the so-called nuclear hyperfine interaction, may shift the nuclear energy levels, as is the case in the electric monopole interaction, or split degenerate states, as afforded by the electric quadrupole interaction and the magnetic dipole interaction. All these three kinds of interactions can be effectively characterized by Mössbauer spectroscopy (MS) through the corresponding hyperfine interactions between the nucleus and the electron shell via particular spectral parameters [65].

MS is particularly suited for investigation of iron-containing materials and for the determination and characterization of their microstructure and magnetic ordering [66]. It can also distinguish non-magnetic and magnetic phases as well as valence state, chemical bond, spin state, internal magnetic field, electric field gradient, lattice vibrations, etc. Diagnostic potential of MS can be effectively used in the study of materials featuring different structural arrangements. Along with crystalline structures—steels with well-defined long-range order [67]—and amorphous structures, investigations of the so-called quasicrystals, which exhibit structural features between these two arrangements, is also possible [68]. Very recently, a new era in the use of the Mössbauer effect has begun, when synchrotron radiation was widely introduced into nuclear resonance scattering experiments [69]. Thus, on-line measurements performed in real time for the study of intermediates during chemical reactions [70] and/or in situ observations of crystallization processes in MGs [71] became feasible.

MS allows unambiguous identification of crystallographic sites in crystalline phases along with distributions of hyperfine interactions between the nuclei and the electron shells in amorphous (i.e., disordered structures), as demonstrated in Figure 1.

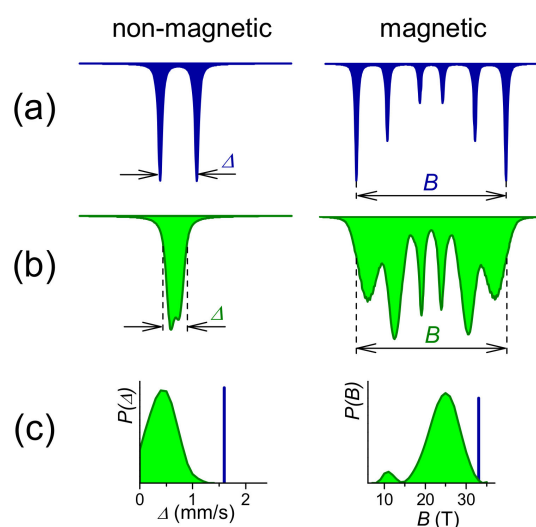


Figure 1. Simulated ^{57}Fe Mössbauer spectra of: (a) Crystalline material; (b) disordered or amorphous material; (c) corresponding hyperfine parameters including quadrupole splitting, Δ , and hyperfine magnetic field, B , together with their distributions $P(\Delta)$ and $P(B)$, respectively.

Crystalline materials exhibit a long-range order translation symmetry due to crystallographic arrangement of the atoms featuring well defined positions, and that is why their Mössbauer spectra consist of narrow lines, the number of which depends upon magnetic states of the ^{57}Fe resonant nuclei, as seen in Figure 1a. The corresponding hyperfine parameters are discrete values comprising quadrupole splitting, Δ , and hyperfine magnetic field, B , for non-magnetic and magnetic samples, respectively. Together with isomer shift, δ , which represents electric monopole interactions, they serve as fingerprints for the identification of the particular crystalline phases. The obtained Mössbauer spectrum shows doublet and sextet of spectral lines, correspondingly, thus information on their magnetic states and relative amounts is also readily available. Detailed description of the individual spectral parameters can be found elsewhere [65].

The situation is quite different when disordered or amorphous materials are analyzed. Here, non-equivalent atomic sites imply that only a short-range order exists in the local atomic arrangement of the resonance atoms. Consequently, the resulting spectral lines are significantly broadened (Figure 1b) and provide distributions of the corresponding hyperfine parameters $P(\Delta)$ and $P(B)$ (Figure 1c).

For the sake of the upcoming discussion, let us also mention that the sextets of Mössbauer lines convey information on the orientation of the net magnetic moment of the inspected sample [72] via mutual ratio of their intensities, which are quantified by the angle Θ . The latter can be derived from the expression $b = (4\sin^2\Theta)/(1 + \cos^2\Theta)$, where b represents relative intensity (area) of the second and/or the fifth spectral line with respect to the first, sixth and the third, fourth lines ($I_1:I_2:I_3:I_4:I_5:I_6 = 3:b:1:1:b:3$). The parameter b can be obtained directly from a spectrum by its evaluation. As shown in Figure 2, Θ is an angle between the vector of net magnetization, M , and the propagation direction of the γ -rays in a Mössbauer effect experiment. It can vary between 0° and 90° , which corresponds to $b = 0$ and $b = 4$, respectively. In a common experimental set-up, γ -rays coming from the Mössbauer radioactive source are (usually) normal to the plane of the absorber (sample). The value $\Theta = 90^\circ$ means that all atomic spins remain within the ribbon plane and so does the net magnetic moment of the sample, while $\Theta = 0^\circ$ indicates that the individual spins are perpendicular to the ribbon plane. In case of randomly oriented spins (e.g., in powder), $\Theta = 54.7^\circ$, the so-called magic angle and $b = 2$.

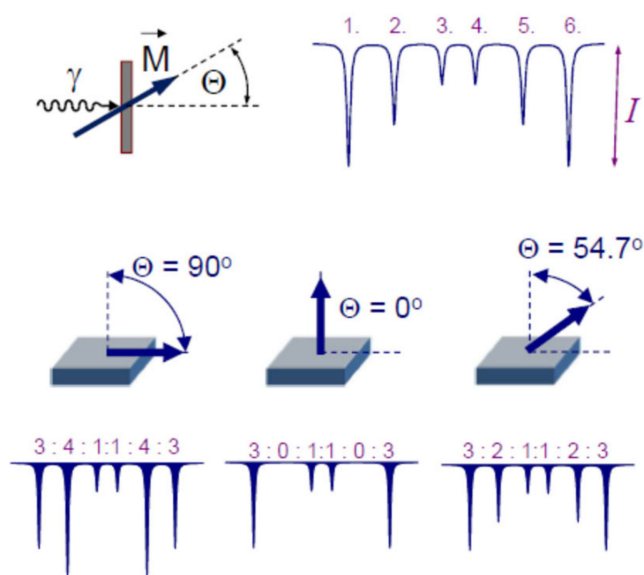


Figure 2. To the explanation of mutual relation between lines intensities of Mössbauer sextet and position of the net magnetic moment of the investigated sample, M , characterized by angle Θ between the sample's plane and direction of gamma rays, γ , from the Mössbauer source.

All Mössbauer effect experiments reported here were accomplished with standard spectrometers equipped with a $^{57}\text{Co}/\text{Rh}$ radioactive source moving with constant acceleration. The absorbers consisted of ~ 1 cm long ribbons that were stacked side-by-side to cover an area of about 1.5 cm^2 . Number of the ribbons depended on their width. Mössbauer spectra were recorded at room temperature and evaluated by NORMOS [73] software. Velocity scale was calibrated with respect to a room-temperature Mössbauer spectrum of a $12.5\text{ }\mu\text{m}$ thick $\alpha\text{-Fe}$ foil.

Broad and overlapping experimental Mössbauer spectra of neutron-irradiated AMAs were fitted to theoretical curves constructed by a histogram method using up to 33 sub-spectra with a fixed linewidth (value taken from the corresponding calibration spectrum of $\alpha\text{-Fe}$ foil). Spectrum asymmetries were covered by introducing correlations between the isomer shift and the hyperfine magnetic and quadrupole interactions, respectively [73]. In this way, distributions of hyperfine magnetic fields, $P(B)$, and quadrupole splittings, $P(\Delta)$, were obtained.

2.2. Investigated Materials

Iron-based amorphous metallic alloys for neutron irradiation experiments were produced by the method of planar flow casting at the Institute of Physics, Slovak Academy of Sciences in Bratislava (courtesy of late P. Duhaj). They were in a form of ribbons with chemical compositions and physical dimensions as compiled in Table 1. The reason for choosing these particular compositions was twofold: (1) They should contain sufficiently high boron content, and (2) they should contain varying amounts of Ni and Cr to assess their role in radiation effects. In addition, chemical composition, which is suitable for formation of NCAs, viz. $\text{Fe}_{73.5}\text{Nb}_3\text{Cu}_1\text{Si}_{13.5}\text{B}_9$, was also considered. On the other hand, Co-containing AMAs were excluded because of potential risk associated with formation of a long-lived ^{60}Co radionuclide after neutron irradiation.

Table 1. Amorphous metallic alloys for neutron irradiation experiments.

Composition	Thickness (μm)	Width (mm)
$\text{Fe}_{80}\text{Cr}_2\text{Si}_4\text{B}_{14}$	~ 30	10
$\text{Fe}_{84}\text{B}_{16}$	~ 30	6
$\text{Fe}_{30}\text{Ni}_{48-x}\text{Cr}_x\text{Mo}_2\text{Si}_5\text{B}_{15}$ ($x = 0, 2, 4, 6, 8$)	16–27	6
$\text{Fe}_{73.5}\text{Nb}_3\text{Cu}_1\text{Si}_{13.5}\text{B}_9$	27	10
$\text{Fe}_{80-x}\text{Ni}_x\text{B}_{20}$ ($x = 10, 20, 30, 40$)	~ 30	5

Neutron irradiation was performed in a nuclear research reactor by a whole neutron spectrum to the total fluences of 10^{14} to 10^{19} n/cm 2 . Ratio of fast to thermal neutrons was nearly 1:1 (contribution of fast neutrons varied in different irradiation experiments between 0.9 and 1.2). Before the irradiation, several approximately 2 cm long pieces of the samples' ribbons were wrapped into an aluminum foil. Temperature during the irradiation did not exceed $70\text{ }^\circ\text{C}$. After the irradiation, the samples were checked for residual activity and, eventually, corresponding gamma spectra were collected [27,61]. Presence of long-lived radionuclides in the samples activated by thermal neutrons had to be considered during preparation and handling the absorbers for Mössbauer effect experiments in order to follow the safety procedures.

3. Results

Modifications of microstructure can be best documented by MS. Representative examples are shown in Figure 3 by Mössbauer spectra of $\text{Fe}_{80}\text{Cr}_2\text{Si}_{14}\text{B}_{14}$ AMA. Experimental points (black squares) are overlaid with theoretically calculated red and blue solid curves in the left-hand part of Figure 3a,b, respectively. In the right-hand side, the corresponding distributions of hyperfine magnetic fields, $P(B)$, are shown. It should be noted that both patterns have the same scales on their respective y-axes.

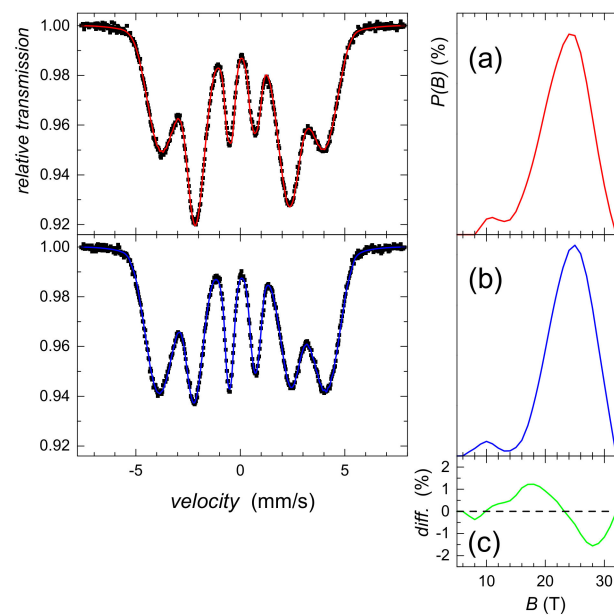


Figure 3. Mössbauer spectra (left) of the $\text{Fe}_{80}\text{Cr}_2\text{Si}_{14}\text{B}_{14}$ amorphous metallic alloy with corresponding distributions of hyperfine magnetic fields, $P(B)$, (right): (a) Non-irradiated sample; (b) after neutron irradiation with a fluence of 10^{19} n/cm²; (c) differences between $P(B)$ distributions.

Changes in $P(B)$ distributions between the non-irradiated and irradiated specimens are highlighted in Figure 3c. Positions of zero differences are denoted by straight dashed lines. Positive differences mean that $P(B)$ of non-irradiated sample prevail that of the irradiated one and vice versa. We have introduced this concept for the sake of better visualization of neutron-irradiation-induced deviations in the whole range hyperfine magnetic fields. Another possibility of assessment of the effects of neutron irradiation rests with inspection of the individual spectral parameters as a function of neutron fluence.

Average hyperfine magnetic field values, $\langle B \rangle$, and standard deviations of $P(B)$ distributions, σ , are plotted against neutron fluence in Figure 4a,b, respectively. Along with the data for $\text{Fe}_{80}\text{Cr}_2\text{Si}_{14}\text{B}_{14}$ AMA also those of $\text{Fe}_{84}\text{B}_{16}$ MG (i.e., without Cr and Si) are plotted for comparison. Mössbauer spectra of $\text{Fe}_{84}\text{B}_{16}$ resemble very much those of $\text{Fe}_{80}\text{Cr}_2\text{Si}_{14}\text{B}_{14}$ and that is why they are not provided here.

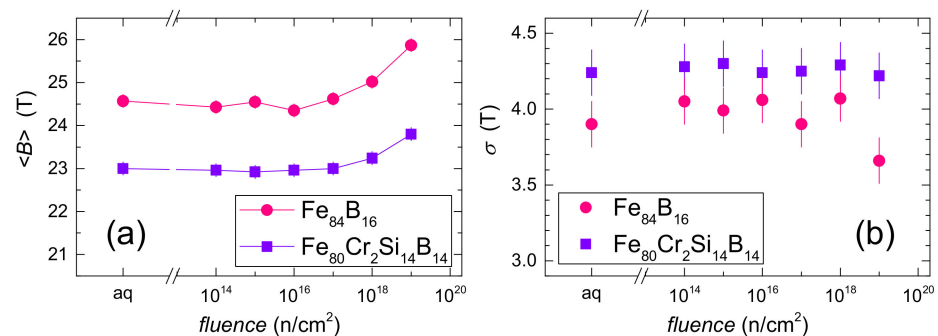


Figure 4. Parameters of distributions of hyperfine magnetic fields, $P(B)$, obtained from Mössbauer spectra of $\text{Fe}_{80}\text{Cr}_2\text{Si}_{14}\text{B}_{14}$ and $\text{Fe}_{84}\text{B}_{16}$, plotted against the neutron fluence: (a) Average hyperfine magnetic field, $\langle B \rangle$; (b) standard deviation, σ .

Positions of the net magnetic moment, that are characterized by an angle Θ , can be derived from line intensities of the Mössbauer spectra (see also Figure 2). In Figure 5, Θ -values obtained from the evaluation of spectra corresponding to $\text{Fe}_{80}\text{Cr}_2\text{Si}_{14}\text{B}_{14}$ and $\text{Fe}_{84}\text{B}_{16}$ AMAs are plotted against the neutron fluence. Random spin orientations are indicated by a green dashed line marking the magic angle of 54.7° .

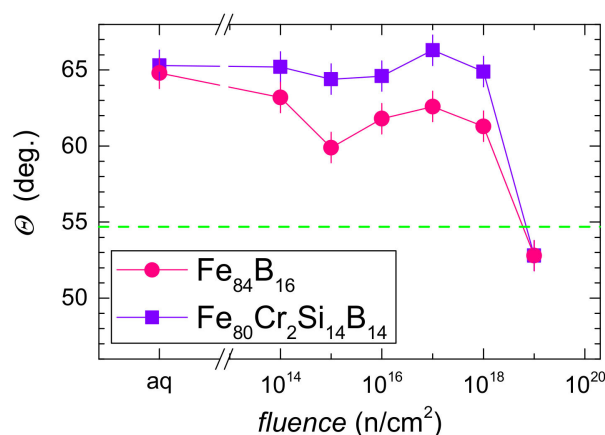


Figure 5. Positions of net magnetic moments characterized by the angle Θ of the $\text{Fe}_{80}\text{Cr}_2\text{Si}_{14}\text{B}_{14}$ and $\text{Fe}_{84}\text{B}_{16}$ plotted against neutron fluence. The green dashed line represents the magic angle (54.7°), which corresponds to random orientation of spins.

A combined effect of chemical composition and neutron irradiation is documented in Figure 6, where Mössbauer spectra of $\text{Fe}_{30}\text{Ni}_{48-x}\text{Cr}_x\text{Mo}_2\text{Si}_5\text{B}_{15}$ AMA are shown for varying contents of Cr, x , both before and after irradiation with 10^{19} n/cm². The scales of the y-axes of 2% apply for spectra corresponding to $x = 0$ up to $x = 8$ before irradiation and 4% belongs to spectra from $x = 8$ after irradiation onwards. As it can be seen, namely this spectrum exhibits pronounced change in both its shape and intensity after neutron irradiation.

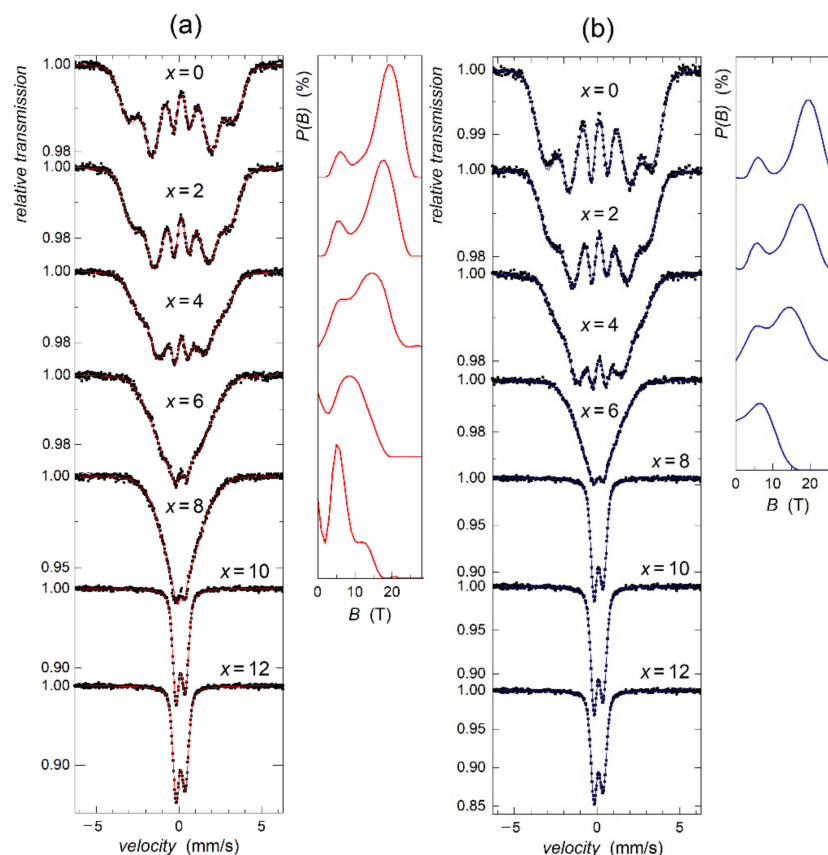


Figure 6. Mössbauer spectra and corresponding $P(B)$ distributions of the $\text{Fe}_{30}\text{Ni}_{48-x}\text{Cr}_x\text{Mo}_2\text{Si}_5\text{B}_{15}$ for the indicated chromium contents, x : (a) In non-irradiated state; (b) after neutron irradiation with a fluence of 10^{19} n/cm².

Average values of hyperfine magnetic fields, $\langle B \rangle$, which were derived from $P(B)$ distributions corresponding to Mössbauer spectra from Figure 6 are plotted in Figure 7 as a function of Cr concentration, x . In the irradiated samples, $\langle B \rangle$ -values for $x > 6$ represent in fact quadrupole splitting values of the corresponding doublets, which are only expressed in units of Tesla for the sake of mutual comparison. Before irradiation, the same situation applies for $x > 8$.

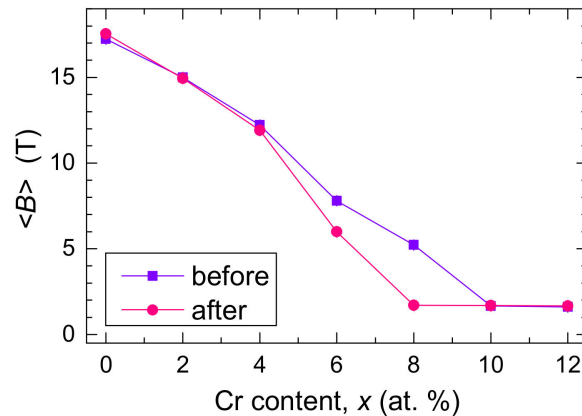


Figure 7. Average hyperfine magnetic fields of $P(B)$ distributions, $\langle B \rangle$ plotted against Cr content, x , as obtained from Mössbauer spectra of the $\text{Fe}_{30}\text{Ni}_{48-x}\text{Cr}_x\text{Mo}_2\text{Si}_5\text{B}_{15}$ amorphous metallic alloy measured before (violet squares) and after (pink circles) neutron irradiation with the fluence of 10^{19} n/cm².

Comparison of $\langle B \rangle$ values derived from Mössbauer spectra of $\text{Fe}_{30}\text{Ni}_{48-x}\text{Cr}_x\text{Mo}_2\text{Si}_5\text{B}_{15}$ AMAs for all Cr concentrations and all neutron fluences is shown in Figure 8 as differences, $\Delta\langle B \rangle = \langle B_{non-irr} \rangle - \langle B_{irr} \rangle$, between non-irradiated samples and the corresponding ones after irradiation with the particular neutron fluence. The range of experimental errors is depicted by dashed lines. While the $x = 0$ sample exhibits a tendency of slight increase in $\langle B \rangle$ towards higher fluences, an opposite and even more pronounced behavior is seen for $x = 6$ and 8. Note that samples with $x = 10$ and $x = 12$ exhibit only pure electric quadrupole interactions and that is why they are not presented in the figure.

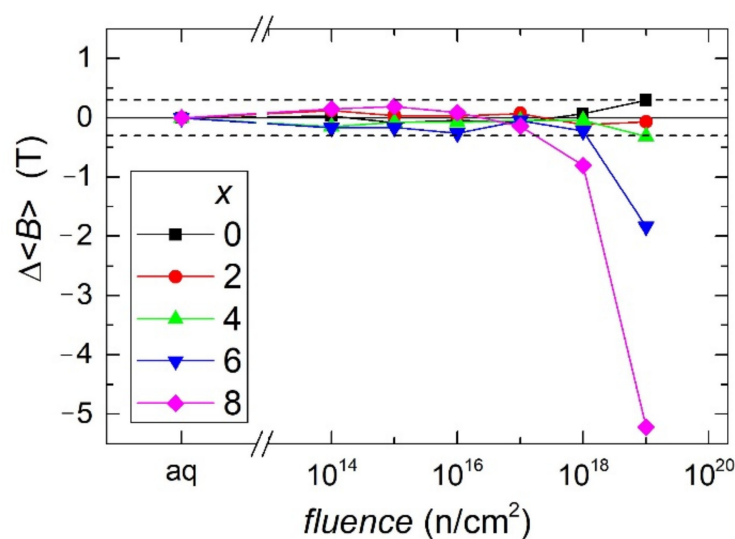


Figure 8. Differences of average hyperfine magnetic fields, $\Delta\langle B \rangle$, between non-irradiated and irradiate $\text{Fe}_{30}\text{Ni}_{48-x}\text{Cr}_x\text{Mo}_2\text{Si}_5\text{B}_{15}$ plotted against the neutron fluence for the indicated Cr contents. Solid lines are only guides to an eye, dashed lines represent the error margin.

Mössbauer spectra of the next investigated system $\text{Fe}_{73.5}\text{Nb}_3\text{Cu}_1\text{Si}_{13.5}\text{B}_9$ are shown in Figure 9 together with corresponding $P(B)$ distributions. This FINEMET composition [74] is suitable for preparation of NCA. That is why this sample was measured both in the original, amorphous state, as well as in nanocrystalline state. The latter was ensured by annealing the original precursor at 540 °C for 1 h in vacuum. Neutron irradiation was accomplished to the total fluence of 3.10^{17} n/cm². Mössbauer spectra of NCAs were fitted with one distribution of hyperfine magnetic fields, $P(B)$, and four individual sextets. The former represents the amorphous residual phase, which is also plotted in Figure 9, whereas the latter is ascribed to the particular sites of $\text{DO}_3\text{-Fe}(\text{Si})$ crystalline phase [75].

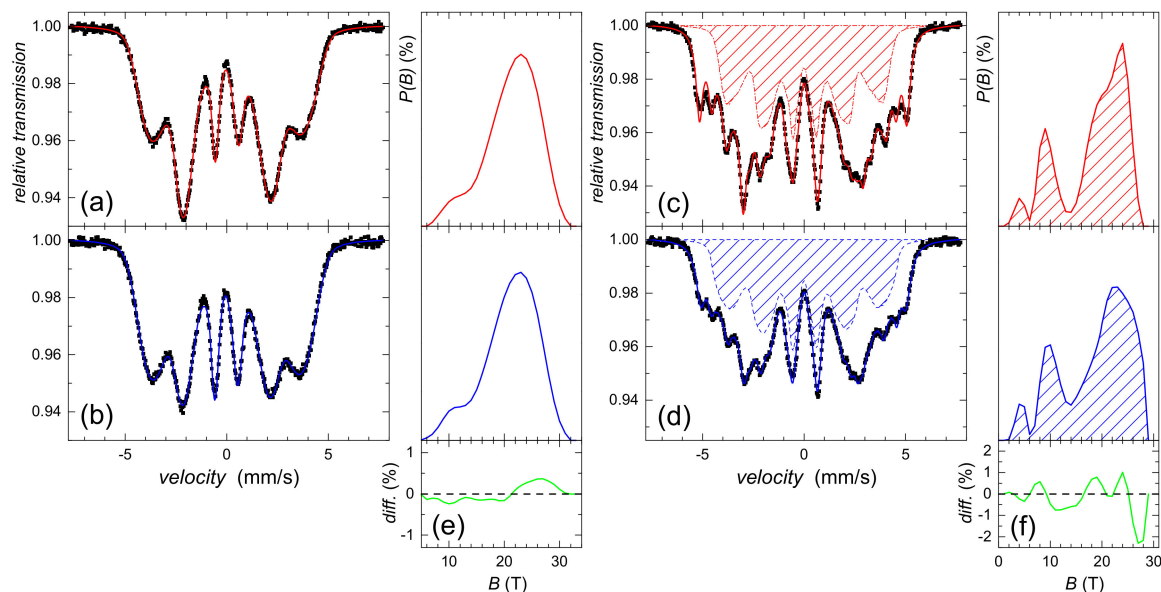


Figure 9. Mössbauer spectra of the $\text{Fe}_{73.5}\text{Nb}_3\text{Cu}_1\text{Si}_{13.5}\text{B}_9$ amorphous metallic alloy with corresponding distributions of hyperfine magnetic fields, $P(B)$: (a) Non-irradiated amorphous sample; (b) amorphous sample after neutron irradiation; (c) non-irradiated nanocrystalline sample; (d) nanocrystalline sample after neutron irradiation; (e) differences between $P(B)$ distributions of amorphous samples; (f) differences between $P(B)$ distributions of nanocrystalline samples. Spectral components representing the amorphous residual phase in nanocrystalline samples are plotted in (c,d).

After neutron irradiation, similar effects as in the previous cases are observed. In the as-quenched AMA, $\langle B \rangle$ increases from 20.5 to 21.0 T, which is only slightly above the experimental error of ± 0.3 T, and the same holds for σ -values of 4.7 and 4.9 T, respectively. Again, a strong tendency of the net magnetic moment to rotate out of the ribbon plane (by $\sim 7^\circ$) can be seen in the respective Mössbauer spectra in Figure 9a,b.

As far as the amorphous residual phase of the NCA sample is concerned, its relative area increases after irradiation from $\sim 52\%$ to $\sim 58\%$, $\langle B \rangle$ is almost unchanged, 18.4 T versus 18.8 T, and so is σ , providing the values of 6.3 and 6.6 T, respectively.

Finally, let us mention the behavior of $\text{Fe}_{80-x}\text{Ni}_x\text{B}_{20}$ ($x = 10, 20, 30, 40$) after neutron irradiation. This particular composition is characterized by well-developed ferromagnetic structure which provides sextets of Mössbauer lines (not shown), similar to those in Figure 3. Quantification of their corresponding $P(B)$ distributions is presented in Figure 10 by the help of differences in average hyperfine fields, $\Delta\langle B \rangle$, and standard deviations, $\Delta\sigma$. Again, both were calculated by subtracting the individual values obtained from the irradiated samples from those which belong to the original, non-irradiated AMA.

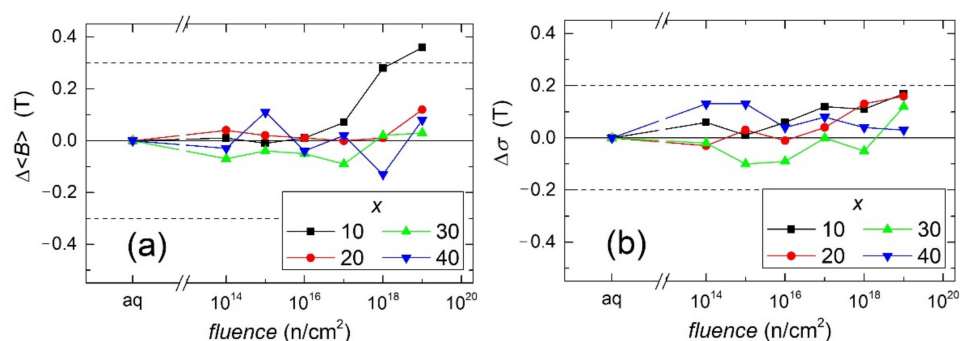


Figure 10. Differences of parameters of distributions of hyperfine magnetic fields, $P(B)$, obtained from Mössbauer spectra of the $\text{Fe}_{80-x}\text{Ni}_x\text{B}_{20}$ amorphous metallic alloy, plotted against neutron fluence for the indicated Ni contents: (a) Average hyperfine magnetic field, $\Delta\langle B \rangle$; (b) standard deviation, $\Delta\sigma$. Solid lines are only guides to an eye, dashed lines represent the error margins.

As for average hyperfine magnetic field, a tendency of its increase with neutron fluence is observed only for the lowest Ni-content ($x = 10$). The other compositions exhibit notable resistance to radiation damage. This is underlined by minute variations in standard deviation over all concentrations and neutron fluences in Figure 10b. It should be noted that the differences in $\langle B \rangle$ and σ fluctuate almost exclusively within their respective error margins which are indicated in both figures by the dashed lines. Thus, in this particular AMA, nickel stabilizes the structure against neutron irradiation.

4. Discussion

Mössbauer spectra in Figure 3 are characteristic for ferromagnetic AMAs and exhibit broadened and overlapped sextets of absorption lines. Nevertheless, it is possible to derive information on the average hyperfine magnetic field, its standard deviation, as well as on the position of the net magnetic moment of the samples, which correlates with intensities of the second and the fifth lines. As it can be seen from Figure 3a,b, after neutron irradiation, a significant decrease of the latter is observed. At the same time, $P(B)$ is shifted toward higher values of the magnetic field.

Notable increase in $\langle B \rangle$ is observed in Figure 4 for both AMAs at fluences higher than 10^{17} n/cm^2 . Standard deviation, σ , of $P(B)$, which is a measure of “disordering”, remains practically unchanged (i.e., within the limits of its experimental errors) for $\text{Fe}_{80}\text{Cr}_2\text{Si}_{14}\text{B}_{14}$ AMA, whereas, in case of $\text{Fe}_{84}\text{B}_{16}$, a slight increase is observed just after irradiation and a tendency to drop to smaller values is revealed at the fluences of 10^{17} n/cm^2 and higher.

In $\text{Fe}_{80}\text{Cr}_2\text{Si}_{14}\text{B}_{14}$ AMA, remarkable re-alignment of spins occurs only after irradiation with neutron fluence higher than 10^{18} n/cm^2 (Figure 5). Spins are rotated from their original positions ($\Theta \sim 65^\circ$) through random orientations, which are marked by a green dashed line, towards slightly out-of-plane arrangements ($\Theta \sim 53^\circ$). A change of more than 12° is observed after neutron irradiation with the fluence of 10^{19} n/cm^2 .

In $\text{Fe}_{84}\text{B}_{16}$ AMA, a tendency of spin rotation starts after neutron irradiation even with the lowest fluency and finishes almost at the same position as in $\text{Fe}_{80}\text{Cr}_2\text{Si}_{14}\text{B}_{14}$. Both systems exhibit similar behavior despite different chemical compositions. Comparable effects were observed also in $\text{Fe}_{73.5}\text{Nb}_3\text{Cu}_1\text{Si}_{13.5}\text{B}_9$ AMA in as-quenched state exposed to neutron irradiation with only 3×10^{17} n/cm^2 . However, presence of Cr in $\text{Fe}_{80}\text{Cr}_2\text{Si}_{14}\text{B}_{14}$ seems to stabilize the structure against radiation damage, as seen from negligible deviations of its standard deviation in Figure 4b. In another composition—Si-free $\text{Fe}_{79}\text{Cu}_1\text{Nb}_7\text{B}_{13}$ —the net magnetic moment rotates after irradiation with fast neutrons in an opposite way (i.e., towards the ribbon plane) [76].

Shapes of Mössbauer spectra in Figure 6 before and after neutron irradiation exhibit remarkable changes. Progressive disappearance of exchange interactions with increasing chromium content is visible in non-irradiated specimens in Figure 6a. Originally magnetically split spectrum for $x = 0$ (characterized by a sextet) gradually vanishes and transforms

into a doublet-like spectral shape for $x = 8$. Electric quadrupole interactions of the latter start to prevail and the V-shaped spectrum looks quite different. The transformation from partially ferromagnetic to fully paramagnetic state, as observed in this sample, is caused by structural modifications initiated by neutron irradiation. Samples $x = 10$ and $x = 12$ are fully paramagnetic even before the neutron irradiation and their Mössbauer spectra exhibit broadened doublets. This effect is on account of differences in chemical composition of these particular AMAs.

In case of low Cr concentrations, differences in spectral shapes before and after neutron irradiation are not so pronounced. Conversion of spectral shapes in the neutron-irradiated AMAs is clearly visible in Figure 6b for $x = 6$ onwards and, eventually, it develops into a well-established doublet for $x = 8$. Here, only pure electric quadrupole interactions exist and this sample becomes fully paramagnetic after neutron irradiation (compare also simulated spectra in Figure 1). Thus, structural rearrangement of atoms induced by neutron irradiation has caused collapse of ferromagnetic exchange interactions at this particular chemical composition of the $\text{Fe}_{30}\text{Ni}_{48-x}\text{Cr}_x\text{Mo}_2\text{Si}_5\text{B}_{15}$ AMA. This is a nice example of how magnetic microstructure can be tailored with a suitable chemical composition and/or neutron irradiation induced structural modification.

Quantification of the above mentioned phenomena is shown in Figure 7 by evolution of average hyperfine magnetic fields, $\langle B \rangle$, with Cr concentration, x , before and after neutron irradiation of the $\text{Fe}_{30}\text{Ni}_{48-x}\text{Cr}_x\text{Mo}_2\text{Si}_5\text{B}_{15}$ AMA with the highest neutron fluence. Up to $x = 4$, $\langle B \rangle$ values do not differ one from another within the error range. For higher Cr concentrations, hyperfine magnetic fields of the irradiated samples decrease more rapidly than in the non-irradiated ones, with a complete collapse of hyperfine magnetic fields (i.e., $\langle B \rangle = 0$ T for $x = 8$). One could expect complete transformation after neutron irradiation from (partially magnetic) into pure paramagnetic state takes place somewhere between Cr-content of 6 and 8. However, because such composition was not available, this part of the curve in Figure 7 is simply connected by a straight line. Preparation of sample with intermediate composition would shed more light upon compositional- and irradiation-induced magnetic transition in this AMA.

Modifications of microstructure with neutron irradiation result in deviations in $\langle B \rangle$ -values as demonstrated by the help of differences between original non-irradiated sample and the ones after irradiation which are shown in Figure 8. Clear distinctions in $\Delta\langle B \rangle$ -values can be seen with respect to the chemical composition of the studied samples. While for $x = 0$ the hyperfine fields slightly increase, completely opposite behavior is found for $x = 6$ and beyond.

Radiation effects in $\text{Fe}_{73.5}\text{Nb}_3\text{Cu}_1\text{Si}_{13.5}\text{B}_9$ in amorphous state are comparable with those in $\text{Fe}_{80}\text{Cr}_2\text{Si}_{14}\text{B}_{14}$ AMA irradiated with lower fluences as far as $\langle B \rangle$, σ , and Θ parameters are concerned. Differences in $P(B)$ in Figure 9e are notably smaller, too. Note that neutron fluence of only $3 \cdot 10^{17}$ n/cm² was applied. Nanocrystalline counterpart of this system exhibits remarkably smaller $\langle B \rangle$ -values of the residual amorphous phase. This might be caused by formation of regions enriched in Cu, Nb, and B because these elements are poorly soluble in $\text{DO}_3\text{-Fe(Si)}$ structure. In addition, regions depleted in Fe and Si, which form the nanocrystals, should be also considered. Consequently, $P(B)$ in Figure 9c exhibits a more complex shape than in fully amorphous sample (Figure 9a). Presence of nanocrystals is indicated in Figure 9c,d by sharp absorption lines superimposed upon broad signal of the residual amorphous phase.

After neutron irradiation, small increase in relative content of the amorphous residuum is observed. This is presumably due to partial amorphization of the nanocrystalline phase. Other spectral parameters associated with nanocrystals do not considerably change. In this respect, it should be reminded that saturation magnetostriction of FINEMET drops from its high positive value in amorphous state to almost zero after nanocrystallization [74]. Thus, the neutron-irradiation-induced changes are not so pronounced [34].

Comparison of differences $\Delta\langle B \rangle$ and $\Delta\sigma$ as a function of neutron fluence are shown in Figure 10 for various compositions of the $\text{Fe}_{80-x}\text{Ni}_x\text{B}_{20}$ AMA. Again, weak dependence

upon Ni-content can be seen showing slight increase of $\Delta\langle B \rangle$ for $x = 10$. Standard deviations exhibit little deviations that are within the error range.

Summarizing the results obtained from neutron irradiation of AMAs with different compositions, the radiation effects revealed by Mössbauer spectrometry comprise changes in average hyperfine magnetic field, $\langle B \rangle$, orientation of net magnetic moment, quantified by angle Θ , and standard deviation of hyperfine distribution, σ . All of them are closely related to local SRO and have implications towards macroscopic—mainly magnetic—parameters. It should be noted; however, that all of them depend upon chemical composition as well as relative concentration of particular elements. Mainly this parameter is responsible for whether the observed changes will be in one or the other direction, viz. increase versus decrease.

During neutron irradiation, dynamic collective displacements of atoms takes place which can be characterized by atomic-to-cluster structural changes as derived from numerical calculations. Displacements can cause changes of the coordination numbers, atom packing efficiency, cluster distribution and regularity [77]. Irradiation also causes energy distribution among the atoms which eventually leads to thermal spikes when significant increase in temperature occurs in regions ~ 10 nm in size [78]. Still, AMAs exhibit specific structural responses to neutron irradiation featuring structural relaxation by rearrangement of free volumes which strongly depends on constituent elements [79]. Thus, the main radiation damage in metals is represented by amorphization, radiation hardening and embrittlement, increase in volume (swelling) and transmutation of radioactive nuclides [80]. All these effects are supposed to modify the local SRO which, in turn, alters also the magnetic microstructure with consequences towards macroscopic (magnetic) parameters.

For example, decrease in Curie temperature T_C obtained from ac susceptibility measurements was observed after neutron irradiation in the same $\text{Fe}_{30}\text{Ni}_{48-x}\text{Cr}_x\text{Mo}_2\text{Si}_5\text{B}_{15}$ AMA as studied here [32,37,81]. It was attributed to neutron-irradiation-induced changes in atomic SRO around the magnetic atoms which lead to changes in Fe-Fe, Fe-Ni, and Fe-Cr correlations in the first peak of the radial distribution function. Increase in Fe-Cr pairs on account of Fe-Ni ones is supposed to be responsible for the observed decrease in T_C [32]. Such situation occurs namely for $x > 4$, which also decreases the $\langle B \rangle$ -values (compare Figure 8). In his particular AMA, one can observe how Cr content affects its phase transition of the second order (i.e., its magnetic microstructure). At certain Cr content ($x \sim 8$), the system becomes so sensitive that it switches from weak magnetic into paramagnetic state after the influence of external factors like (e.g., neutron irradiation) (Figure 7).

The opposite behavior of the effect of neutron irradiation on $\langle B \rangle$ is observed in $x = 0$, when its increasing value suggests rising importance of Fe-Fe and Fe-Ni pairs when no Cr is present. Even more pronounced increase in $\langle B \rangle$ -values is found in $\text{Fe}_{80}\text{Cr}_2\text{Si}_{14}\text{B}_{14}$ AMA, which contains some Cr but also higher amount of Fe (and no Ni). Chromium is moved from its original positions, thus enabling Fe-Fe exchange interactions to become more abundant, which favors the rise of $\langle B \rangle$. In $\text{Fe}_{84}\text{B}_{16}$ AMA, this effect is also seen and it is even more pronounced (Figure 4a).

Another example of radiation-induced modifications of macroscopic magnetic parameters concerns hysteresis loops that were dramatically broadened after neutron irradiation of $\text{Fe}_{80}\text{Cr}_2\text{Si}_{14}\text{B}_{14}$. Consequent increase in coercive field [59] worsens magnetic features of this AMA. This macroscopic parameter is; thus, closely related to the local SRO too.

According to the results of molecular dynamic simulations performed upon ZrCu alloys [82], free volumes, established in amorphous matrix by neutron irradiation, were systematically self-recovered, thus showing excellent resistance to neutron irradiation. In the case of boron-containing AMAs, the situation is different, as confirmed by our experimental results. Here, ^{10}B captures thermal neutrons and through nuclear reaction $^{10}\text{B}(n, \alpha)^7\text{Li}$ produces high-energy α (1.4 MeV) and Li (0.9 MeV) particles. Both belong to heavy particles (ions) and, together with fast neutrons, they are important sources of radiation damage which cause displacements of atoms. It is noteworthy that no changes of average isomer shift values were observed. Consequently, variations of SRO are not of

chemical but topological origin. Indeed, the most pronounced increase in $\langle B \rangle$ was observed in the $\text{Fe}_{84}\text{B}_{16}$ AMA which underlines the contribution of boron to displacements of atoms thorough the above-mentioned nuclear reaction.

In addition, elastic stress centers are produced during neutron irradiation [32] as a result of atom mixing. They originate in the free volume-rich regions produced during irradiation by a rapid collapse of the vacancy-rich core of the displacement cascades [34]. Presence of free volume and its increase after irradiation was confirmed in $\text{Fe}_{30}\text{Ni}_{48-x}\text{Cr}_x\text{Mo}_2\text{Si}_5\text{B}_{15}$ by positron annihilation spectroscopy [56]. Presumably, stress centers also contribute to re-positioning of magnetic moments of the individual resonant nuclei so that the net magnetization vector tends to turn out from its original position. Because of shape anisotropy and resulting domain structure [83,84] influenced by preparation conditions, the net magnetic moment in as-quenched ribbons acquires a close-to-plane orientation. Stress centers can also cause the domain walls pinning as they originate mostly in free-volume regions formed during irradiation in AMAs [61]. The manner in which the spins move from their original position depends upon local stresses and magnetostriction of the sample. Positive magnetostriction in combination with compressive stress implies out-of-plane movement of the spins, while the negative one acts in an opposite way [85].

Modification of SRO can be quantified by the help of standard deviation, σ , of the corresponding distributions of hyperfine magnetic fields, $P(B)$. Alternations in σ are directly related to changes in the local microstructure. Interestingly, even though the magnetic microstructure is affected, in some cases almost no effects upon the overall ‘disorder’—change in σ —are observed. This can be explained by rearrangement of atoms within particular atomic pairs. While some exhibit enhanced exchange interactions (Fe-Fe, Fe-Ni), others like Fe-Cr act in an opposite way. Therefore, while the averaged structural positions do not significantly vary, the associated magnetic ordering does. It is noteworthy that the observed changes in σ and $\langle B \rangle$ depend upon composition of the investigated alloys [79]. This can be understood in terms of atom mixing when individual atoms can change their positions and, in this way, they modify the local SRO. Presence of free volume which varies with composition of AMAs [27,57,86] should be also considered. This additionally underlines the importance of combined effects of chemical composition and structural modification, ensured by neutron irradiation upon magnetic microstructure of AMAs in general.

5. Conclusions

Amorphous metallic alloys were considered to be resistant against neutron irradiation, mainly because of their disordered structure that was thought to accommodate possible defects caused by knock-off atoms. As we have demonstrated, rearrangements of atoms even inside an amorphous structure can be effectively unveiled by local probe method of Mössbauer spectrometry. Nevertheless, the extent of the neutron-irradiation-induced modifications strongly depends upon several factors. Among them, chemical composition of the irradiated AMA plays a crucial role. While some systems are rather resistant (e.g., Fe-Ni-B), others show notably pronounced changes in their magnetic microstructure. In this respect it should be mentioned that, even though according to our results the Fe-Ni-B AMA tolerates the neutron irradiation without significant modification of its structure and/or magnetic ordering, its practical applications in radiation-exposed environments are still pending. Especially sensitive are those which exhibit close-to-room magnetic ordering temperature at ambient conditions. Such systems are close to their phase transition of the second order (i.e., their magnetic microstructure is about to be changed as a response to external factors such as temperature or atom mixing). They are, so to say, ‘at the edge’ and, consequently, even the slightest deviation from normal steady state leads to modification of their magnetic behavior. Thus, when such AMAs are exposed to neutron irradiation, they sensitively react to such structural modifications. As an example, the $\text{Fe}_{30}\text{Ni}_{48-x}\text{Cr}_x\text{Mo}_2\text{Si}_5\text{B}_{15}$ with particular content of Cr ($x = 8$) can be mentioned. There are also other compositions (e.g., $\text{Fe}_{76}\text{Mo}_8\text{Cu}_1\text{B}_{15}$ [21]) which demonstrate the same sensitivity

to external factors. Such specially designed AMAs are particularly suited for the study of faint effects of radiation that might be hidden in others.

The next factor to be considered is related to the spectrum of neutrons as well as their energy during irradiation. The same system reacts differently with respect to the total neutron fluence used. Nevertheless, because investigations of neutron-induced effects in AMAs are, in general, pretty rare, this particular point would deserve more attention. It is understandable that access to a nuclear reactor for irradiating the samples is not an easy task. Even when granted, it is quite demanding to ensure particular spectrum of neutrons as well as their fluence. In this respect, alternative sources of neutrons comprising neutron generators or accelerator-based production of (fast) neutrons could be employed.

In the future research of radiation effects in amorphous metallic alloys, which are still the focus of many research groups, one should consider their appropriate chemical composition as well as suitable sources of neutrons. In Part II of this paper, we will focus on radiation effects in amorphous metallic alloys as revealed by Mössbauer spectrometry after ion irradiation.

Funding: This research was funded by the Scientific Grant Agency of the Ministry of Education, Science, Research and Sport of the Slovak Republic, grant number VEGA 1/0130/20, by the Slovak Research and Development Agency, grant number APVV-16-0079, and by the European Regional Development Fund-Project “Center for Advanced Applied Sciences”, grant number CZ.02.1.01/0.0/0.0/16_019/0000778.

Institutional Review Board Statement: Not applicable.

Informed Consent Statement: Not applicable.

Data Availability Statement: Data supporting the reported results can be obtained from the author upon request.

Acknowledgments: Special thanks are given to J. Sitek (Bratislava) and I. Škorvánek (Košice) for fruitful discussions during early stages of this research.

Conflicts of Interest: The author declares no conflict of interest. The funders had no role in the design of the study; in the collection, analyses, or interpretation of data; in the writing of the manuscript, or in the decision to publish the results.

References

1. Huang, E.-W.; Liaw, P.K. High-temperature materials for structural applications: New perspectives on high-entropy alloys, bulk metallic glasses, and nanomaterials. *MRS Bulletin*. **2019**, *44*, 847–853. [[CrossRef](#)]
2. Li, H.; He, A.; Wang, A.; Xie, L.; Li, Q.; Zhao, C.; Zhang, G.; Chen, P. Improvement of soft magnetic properties for distinctly high Fe content amorphous alloys via longitudinal magnetic field annealing. *J. Magn. Magn. Mater.* **2019**, *471*, 110–115. [[CrossRef](#)]
3. Cao, C.C.; Wang, Y.G.; Zhu, L.; Meng, Y.; Zhai, X.B.; Dai, Y.D.; Chen, J.K.; Pan, F.M. Local structure, nucleation sites and crystallization behavior and their effects on magnetic properties of $\text{Fe}_{81}\text{Si}_x\text{B}_{10}\text{P}_{8-x}\text{Cu}_1$ ($x = 0\sim 8$). *Sci. Rep.* **2018**, *8*, 1243. [[CrossRef](#)]
4. Herzer, G. Modern soft magnets: Amorphous and nanocrystalline materials. *Acta Mater.* **2013**, *61*, 718–734. [[CrossRef](#)]
5. McHenry, M.E.; Laughlin, D.E. Nano-scale materials development for future magnetic applications. *Acta Mater.* **2000**, *48*, 223–238. [[CrossRef](#)]
6. Khong, J.C.; Daisenberger, D.; Burca, G.; Kockelmann, W.; Tremsin, A.S.; Mi, J. Design and characterisation of metallic glassy alloys of high neutron shielding capability. *Sci. Rep.* **2016**, *6*, 36998. [[CrossRef](#)]
7. Blink, J.; Farmer, J.; Choi, J.; Saw, C. Applications in the nuclear industry for thermal spray amorphous metal and ceramic coatings. *Metal. Mater. Trans. A* **2009**, *40*, 1344–1354. [[CrossRef](#)]
8. Spiller, P.; Blasche, K.; Franczak, B.; Kirk, M.; Hülsmann, P.; Omet, C.; Ratschow, S.; Stadlmann, J. Accelerator plans at GSI for plasma physics applications. *Nucl. Instr. Meth. A* **2005**, *544*, 117–124. [[CrossRef](#)]
9. Han, J.; Hong, J.; Kwon, S.; Choi-Yim, H. Effect of Cr Addition on Magnetic Properties and Corrosion Resistance of Optimized Co and Fe-Based Amorphous Alloys. *Metals* **2021**, *11*, 304. [[CrossRef](#)]
10. Pei, L.; Zhang, X.; Yuan, Z. Reduction and immobilization of movable Cu^{2+} ions in soils by $\text{Fe}_{78}\text{Si}_9\text{B}_{13}$ amorphous alloy. *Metals* **2021**, *11*, 310. [[CrossRef](#)]
11. Kozejova, D.; Fecova, L.; Klein, P.; Sabol, R.; Hudak, R.; Sulla, I.; Mudronova, D.; Galik, J.; Varga, R. Biomedical applications of glass-coated microwires. *J. Magn. Magn. Mater.* **2019**, *470*, 2–5. [[CrossRef](#)]
12. Priezev, N.V. Cooling under applied stress rejuvenates amorphous alloys and enhances their ductility. *Metals* **2021**, *11*, 67. [[CrossRef](#)]

13. Zhai, X.B.; Wang, Y.G.; Zhu, L.; Zheng, H.; Dai, Y.D.; Chen, J.K.; Pan, F.M. Influence of Ni substitution for B on crystallization behavior, microstructure and magnetic properties of FeBCu alloys. *J. Magn. Magn. Mat.* **2019**, *480*, 47–52. [[CrossRef](#)]
14. Han, J.; Kwon, S.; Sohn, S.; Schroers, J.; Choi-Yim, H. Optimum soft magnetic properties of the FeSiBNbCu alloy achieved by heat treatment and tailoring B/Si ratio. *Metals* **2020**, *10*, 1297. [[CrossRef](#)]
15. Meylan, C.M.; Papparotto, F.; Nachum, S.; Orava, J.; Miglierini, M.; Basykh, V.; Ferenc, J.; Kulik, T.; Greer, A.L. Simulation of shear-transformation zones in metallic glasses by cryogenic thermal cycling. *J. Non-Cryst. Sol.* **2020**, *548*, 120299. [[CrossRef](#)]
16. Perea, D.; Parra, C.; Ramasamy, P.; Stoica, M.; Eckert, J.; Bolívar, F.; Echeverría, F. Structural and phase evolution upon annealing of Fe₇₆Si_{9-x}B₁₀P₅Mo_x (x = 0, 1, 2 and 3) alloys. *Metals* **2020**, *10*, 881. [[CrossRef](#)]
17. Butvinová, B.; Butvin, P.; Mat'ko, I.; Švec Sr., P.; Kadlečiková, M. Impact of surfaces on the magnetic properties of Fe-based nanocrystalline ribbons. *Appl. Surf. Sci.* **2021**, *538*, 147942. [[CrossRef](#)]
18. Aronin, A.; Abrosimova, G. Specific features of structure transformation and properties of amorphous-nanocrystalline alloys. *Metals* **2020**, *10*, 358. [[CrossRef](#)]
19. Slugeň, V.; Soják, S.; Egger, W.; Kršjak, V.; Šimeg Veterníková, J.; Petriska, M. Radiation Damage of Reactor Pressure Vessel Steels Studied by Positron Annihilation Spectroscopy—A Review. *Metals* **2020**, *10*, 1378. [[CrossRef](#)]
20. Shkapa, V.M.; Shalaev, A.M.; Polotnjuk, V.V.; Likhtorovich, S.P.; Nemoshkalenko, V.V.; Kotov, V.V. Positron, Mössbauer and NMR studies of γ -irradiated FeCoB metallic glass. *J. Non-Cryst. Sol.* **1993**, *155*, 90–94. [[CrossRef](#)]
21. Miglierini, M.; Schaaf, P.; Škorvánek, I.; Janičkovič, D.; Carpena, E.; Wagner, S. Laser-induced structural modifications of FeMoCuB metallic glasses before and after transformation into a nanocrystalline state. *J. Phys. Condens. Matter.* **2001**, *13*, 10359–10369. [[CrossRef](#)]
22. Kane, S.N.; Satalkar, M.; Ghosh, A.; Shah, M.; Ghodke, N.; Pramod, R.; Sinha, A.K.; Singh, M.N.; Dwivedi, J.; Coisson, M.; et al. Electron-irradiation induced changes in structural and magnetic properties of Fe and Co based metallic glasses. *J. Alloy. Compd.* **2014**, *615*, S324–S327. [[CrossRef](#)]
23. Butvinová, B.; Butvin, P.; Janotová, I.; Janičkovič, D.; Sitek, J.; Dekan, J.; Holková, D.; Mat'ko, I. Magnetic response of amorphous and nanocrystalline FeSn(P)B ribbons to electron irradiation. *Acta Phys. Pol. A* **2020**, *137*, 839–842. [[CrossRef](#)]
24. Miglierini, M.; Lančok, A.; Pavlovič, M. CEMS studies of structural modifications of metallic glasses by ion bombardment. *Phys. Met. Metall.* **2010**, *109*, 469–474. [[CrossRef](#)]
25. Kuzmann, E.; Lakatos-Varsanyi, M.; Nomura, K.; Ujihira, Y.; Masumoto, T.; Principi, G.; Tosello, C.; Havancsák, K.; Vértes, A. Combination of electrochemical hydrogenation and Mössbauer spectroscopy as a tool to show the radiation effect of energetic heavy ions in Fe–Zr amorphous alloys. *Electrochem. Commun.* **2000**, *2*, 130–134. [[CrossRef](#)]
26. Violet, C.E.; Borg, R.J.; May, L.; Rao, K.V.; Nagues, J.; Taylor, R.D.; Batra, A.P. Magnetic behavior of amorphous Fe-Ni-Zr alloys and their response to radiation damage. *Hyperfine Inter.* **1988**, *42*, 963–966. [[CrossRef](#)]
27. Sitek, J.; Miglierini, M.; Balúch, S. Post Irradiation Activity of FeNiB Metallic Glasses. In *Key Engineering Materials*; Duhaj, P., Mrafko, P., Švec, P., Eds.; Trans. Tech. Publications: Bäch, Switzerland, 1990; Volume 40, pp. 275–279. [[CrossRef](#)]
28. Zentko, A.; Timko, M.; Duhaj, P.; Škorvánek, I. The effect of neutron irradiation on the electrical resistivity of amorphous Fe₄₇Ni₂₅Si₁₀ alloys. *Phys. Status Solidi. A Appl. Res.* **1981**, *64*, K19–K22. [[CrossRef](#)]
29. Zentko, A.; Timko, M.; Duhaj, P. Effect of neutron irradiation on the magnetic properties of amorphous Fe₇₄Ni₂₅B₁₈Si₁₀ alloys. *Phys. Status Solidi. A Appl. Res.* **1981**, *66*, K125–K126. [[CrossRef](#)]
30. Zentko, A.; Frait, Z.; Duhaj, P. Ferromagnetic resonance in neutron irradiated amorphous Fe₇₄Ni₂₅B₁₈Si₁₀ alloys. *Czech. J. Phys. B* **1982**, *32*, 359–362. [[CrossRef](#)]
31. Škorvánek, I.; Zentko, A. Effects of neutron irradiation on magnetic properties of Fe₈₀B₂₀ amorphous alloys. *Phys. Status Solidi. A Appl. Res.* **1987**, *99*, 275–278. [[CrossRef](#)]
32. Škorvánek, I.; Idzikowski, B.; Zentko, A.; Mosiniewicz-Szablewska, E. Influence of neutron irradiation on the magnetic properties of FeNiCrMoSiB amorphous alloys. *Phys. Status Solidi. A Appl. Res.* **1988**, *108*, 747–751. [[CrossRef](#)]
33. Mihalik, M.; Kováč, J.; Zentko, A.; Lovas, A. Some Magnetic Properties of Neutron Irradiated Fe_{85-x}Cr_xB₁₅ Metallic Glasses. *Phys. Status Solidi. A Appl. Res.* **1989**, *114*, 679–684. [[CrossRef](#)]
34. Škorvánek, I.; Zentko, A.; Uličiansky, S. Influence of neutron irradiation on the coercive field of some iron-based amorphous alloys. *Acta Phys. Pol.* **1989**, *A76*, 171–175.
35. Macko, L.; Mihalik, M.; Kováč, J.; Zentko, A. Magnetization studies of Cr concentration and neutron irradiation effects in Fe₃₀Ni_{48-x}Cr_xMo₂Si₅B₁₅ amorphous alloys. *Phys. Status Solidi. A Appl. Res.* **1991**, *124*, 533–539. [[CrossRef](#)]
36. Gerling, R.; Schimansky, F.P.; Wagner, R. Restoration of the ductility of thermally embrittled amorphous alloys under neutron irradiation. *Acta Metall.* **1987**, *35*, 1001–1006. [[CrossRef](#)]
37. Škorvánek, I.; Gerling, R.; Miglierini, M.; Zentko, A.; Seberini, M. Structural Relaxation in Neutron Irradiated FeNiCrMoSiB Metallic Glasses. *Key Eng. Mater.* **1993**, *81–83*, 587–592.
38. Illeková, E.; Janičkovič, D.; Miglierini, M.; Škorvánek, I.; Švec, P. Influence of Fe/B Ratio on Thermodynamic Properties of Amorphous Fe-Mo-Cu-B. *J. Magn. Magn. Mat.* **2006**, *304*, e636–e638. [[CrossRef](#)]
39. Škorvánek, I.; Gerling, R. The influence of neutron irradiation on the soft magnetic and mechanical properties of amorphous and nanocrystalline Fe_{73.5}Cu₁Nb₃Si_{13.5}B₉ alloys. *J. Appl. Phys.* **1992**, *72*, 3417–3422. [[CrossRef](#)]
40. Škorvánek, I.; Gerling, R.; Graf, T.; Fricke, M.; Hesse, J. Neutron Irradiation effects on the structural, magnetic and mechanical properties of amorphous and nanocrystalline Fe_{73.5}Cu₁Nb₃Si_{13.5}B₉. *IEEE Trans. Magn.* **1994**, *30*, 548–551. [[CrossRef](#)]

41. Sitek, J.; Miglierini, M. Mössbauer Spectroscopy on Amorphous $\text{Fe}_x\text{Ni}_{80-x}\text{B}_{20}$ after Neutron Irradiation. *Phys. Status Solidi. A Appl. Res.* **1985**, *89*, K31–K33. [[CrossRef](#)]
42. Zentko, A.; Škorvánek, I.; Eremenko, V.V.; Checherskii, V.D. Mössbauer study of neutron irradiated $\text{Fe}_{60}\text{Ni}_{40}\text{B}_{20}$ amorphous alloys. *Phys. Status Solidi. A Appl. Res.* **1986**, *93*, K161–K164. [[CrossRef](#)]
43. Habibi, S.; Gupta, A.; Principi, G. Thermal neutron irradiation of Fe-Si-B glasses. *Hyperfine Interact.* **1991**, *69*, 623–626. [[CrossRef](#)]
44. Gupta, A.; Habibi, S.; Principi, G. Neutron irradiation effects in metallic glasses. *Mater. Sci. Eng. A* **1991**, *134*, 992–995. [[CrossRef](#)]
45. Sitek, J.; Miglierini, M.; Lipka, J.; Tóth, I. Study of Fe-Ni-Cr-Mo-Si-B Metallic Glasses after Neutron Irradiation. *Hyperfine Interact.* **1991**, *69*, 713–716. [[CrossRef](#)]
46. Gupta, A.; Habibi, S.; Principi, G. Study of short range order in Fe-Ni-Si-B amorphous alloys. *Mater. Sci. Eng.* **2001**, *A304–306*, 1058–1061. [[CrossRef](#)]
47. Škorvánek, I.; Miglierini, M.; Duhaj, P. Magnetism and Mössbauer spectroscopy in nanocrystalline FeNbCrCuB alloy. In *Materials Science Forum*; Fiorani, D., Magini, M., Eds.; Trans. Tech. Publications: Bäch, Switzerland, 1997; Volumes 235–238, pp. 771–776. [[CrossRef](#)]
48. Miglierini, M.; Škorvánek, I.; Grenèche, J.-M. Microstructure and hyperfine interactions of the $\text{Fe}_{73.5}\text{Nb}_{4.5}\text{Cr}_5\text{CuB}_{16}$ nanocrystalline alloys: Mössbauer effect temperature measurements. *J. Phys. Condens. Matter.* **1998**, *10*, 3159–3176. [[CrossRef](#)]
49. Miglierini, M.; Sitek, J.; Szász, Z.; Vitáček, K. ^{57}Fe Mössbauer Study of Amorphous and Nanocrystalline $\text{Fe}_{73.5}\text{Nb}_3\text{Cu}_1\text{Si}_{13.5}\text{B}_9$ After Neutron Irradiation. *Hyperfine Interact.* **1994**, *84*, 295–299. [[CrossRef](#)]
50. Sitek, J.; Tóth, I.; Degmová, J.; Uváčik, P. Nanocrystalline alloys of Fe-Cu-Nb-Si-B after neutron irradiation. *Czech. J. Phys.* **1997**, *47*, 523–527. [[CrossRef](#)]
51. Sitek, J.; Seberíni, M.; Tóth, I.; Degmová, J.; Uváčik, P. Neutron irradiation effect on amorphous and nanocrystalline FeZrB(Cu) at low temperature. *Mater. Sci. Eng. A* **1997**, *226–228*, 574–576. [[CrossRef](#)]
52. Sitek, J.; Degmová, J. External influence on the FINEMET nanocrystals. *Czech. J. Phys.* **2001**, *51*, 727–733. [[CrossRef](#)]
53. Degmová, J.; Sitek, J.; Grenèche, J.-M. Some magnetic properties of nanoperm alloy after irradiation. *Czech. J. Phys.* **2001**, *51*, 703–710. [[CrossRef](#)]
54. Sitek, J.; Dekan, J.; Pavlovič, M. Radiation damage of Fe-based nanocrystalline materials. *Acta Phys. Pol. A* **2014**, *126*, 84–85. [[CrossRef](#)]
55. Miglierini, M.; Sitek, J. Neutron Irradiation of Metallic Glasses and Mössbauer Spectroscopy. In *Key Engineering Materials*; Duhaj, P., Mrafko, P., Švec, P., Eds.; Trans. Tech. Publications: Bäch, Switzerland, 1990; Volumes 40–41, pp. 281–285. [[CrossRef](#)]
56. Miglierini, M.; Sitek, J.; Macko, L.; Mihalik, M.; Zentko, A. Mössbauer Spectroscopy and Additional Study of Neutron Irradiated Cr-doped Metallic Glasses. *Hyperfine Interact.* **1990**, *60*, 695–698. [[CrossRef](#)]
57. Miglierini, M.; Sitek, J.; Balúch, S.; Cirák, J.; Lipka, J. Short-range Order of Amorphous FeNiB Alloys after Neutron Irradiation. *Hyperfine Interact.* **1990**, *55*, 1037–1041. [[CrossRef](#)]
58. Miglierini, M. Mössbauer Study of Neutron Irradiated FeNiCrMoSiB Metallic Glass. *Phys. Rev. B* **1991**, *44*, 7225–7233. [[CrossRef](#)] [[PubMed](#)]
59. Miglierini, M.; Škorvánek, I. Magnetic Study of Neutron Irradiated FeCrSiB Metallic Glass. *Mater. Sci. Eng. A* **1991**, *147*, 101–106. [[CrossRef](#)]
60. Miglierini, M.; Nasu, S.; Sitek, J. Influence of Neutron Irradiation on Ferromagnetic Metallic Glasses. *Hyperfine Interact.* **1992**, *70*, 885–888. [[CrossRef](#)]
61. Miglierini, M.; Škorvánek, I.; Nasu, S.; Sitek, J. Neutron Irradiation Effects on Magnetic Properties of Fe-based Ferromagnetic Metallic Glasses. *Mater. Trans. JIM* **1992**, *33*, 327–336. [[CrossRef](#)]
62. Yang, L.; Li, H.Y.; Wang, P.W.; Wu, S.Y.; Guo, G.Q.; Liao, B.; Guo, Q.L.; Fan, X.Q.; Huang, P.; Lou, H.B.; et al. Structural responses of metallic glasses under neutron irradiation. *Sci. Rep.* **2017**, *7*, 16739. [[CrossRef](#)]
63. Brechtel, J.; Wang, H.; Kumar, N.A.P.K.; Yang, T.; Lin, Y.-R.; Bei, H.; Neuefeind, J.; Dmowski, W.; Zinkle, S.J. Investigation of the thermal and neutron irradiation response of BAM-11 bulk metallic glass. *J. Nucl. Mater.* **2019**, *526*, 151771. [[CrossRef](#)]
64. Xiong, F.; Li, M.; Yang, L. Effective self-healing behavior of amorphous-nanocrystalline alloy under neutron irradiation. *Comp. Mater. Sci.* **2020**, *176*, 109532. [[CrossRef](#)]
65. Nasu, S. General Introduction to Mössbauer Spectroscopy. In *Mössbauer Spectroscopy, Tutorial Book*; Yoshida, Y., Langouche, G., Eds.; Springer-Verlag: Berlin Heidelberg, Germany, 2013; pp. 1–22. [[CrossRef](#)]
66. Principi, G. The Mössbauer effect: A romantic scientific page. *Metals* **2020**, *10*, 992. [[CrossRef](#)]
67. Grgač, P.; Moravčík, R.; Kusý, M.; Tóth, I.; Miglierini, M.; Illeková, E. Thermal stability of metastable austenite in rapidly solidified chromium-molybdenum-vanadium tool steel powder. *Mater. Sci. Eng. A* **2004**, *375–377*, 581–584. [[CrossRef](#)]
68. Nasu, S.; Miglierini, M.; Ishihara, K.N.; Shingu, P.H. Transformation from icosahedral quasicrystalline to amorphous structure in $\text{Al}_{65}\text{Cu}_{20}\text{Fe}_{15}$. *J. Phys. Soc. Jpn.* **1992**, *61*, 3766–3772. [[CrossRef](#)]
69. Rüffer, R.; Chumakov, A.I. Historical developments and future perspectives in nuclear resonance scattering. In *Modern Mössbauer Spectroscopy, New Challenges Based on Cutting-Edge Techniques*; Yoshida, Y., Langouche, G., Eds.; Springer Nature Singapore Pte Ltd.: Singapore, 2021; pp. 1–55. [[CrossRef](#)]
70. Machala, L.; Procházka, V.; Miglierini, M.; Sharma, V.K.; Marušák, Z.; Wille, H.-C.; Zbořil, R. Direct evidence of Fe(V) and Fe(IV) intermediates during reduction of Fe(VI) to Fe(III): A nuclear forward scattering of synchrotron radiation approach. *Phys. Chem. Chem. Phys.* **2015**, *17*, 21787–21790. [[CrossRef](#)]

71. Miglierini, M.; Procházka, V.; Ruffer, R.; Zbořil, R. In situ crystallization of metallic glasses during magnetic annealing. *Acta Mater.* **2015**, *91*, 50–56. [[CrossRef](#)]
72. Gütlich, P.; Bill, E.; Trautwein, A.X. *Mössbauer Spectroscopy and Transition Metal Chemistry, Fundamentals and Applications*; Springer: Berlin/Heidelberg, Germany, 2011; pp. 113–118. [[CrossRef](#)]
73. Brand, R.A. Improving the validity of hyperfine field distributions from magnetic alloys: Part I: Unpolarized source. *Nucl. Instr. Meth. Phys. Res. B* **1987**, *28*, 398–416. [[CrossRef](#)]
74. Yoshizawa, Y.; Oguma, S.; Yamauchi, K. New Fe-based soft magnetic alloys composed of ultrafine grain structure. *J. Appl. Phys.* **1988**, *64*, 6044–6046. [[CrossRef](#)]
75. Hampel, G.; Pundt, A.; Hesse, J. Crystallization of $\text{Fe}_{73.5}\text{Cu}_1\text{Nb}_3\text{Si}_{13.5}\text{B}_9$ structure and kinetics examined by X-ray diffraction and Mössbauer effect spectroscopy. *J. Phys. Condens. Matter.* **1992**, *4*, 3195–3200. [[CrossRef](#)]
76. Miglierini, M.; Cesnek, M.; Štefánik, M. Fast neutron irradiation of boron-containing metallic glass. In Proceedings of the International Conference on the Applications of the Mössbauer Effect, Brasov, Romania, 5–10 September 2021.
77. Dong, Y.; Li, M.; Malomo, B.; Yang, L. Microstructural evolution in ZrCu metallic glass under neutron irradiation. *Comp. Mater. Sci.* **2021**, *188*, 110183. [[CrossRef](#)]
78. Baumer, R.E.; Demkowicz, M.J. Radiation response of amorphous metal alloys: Subcascades, thermal spikes and super-quenched zones. *Acta Mater.* **2015**, *83*, 419–430. [[CrossRef](#)]
79. Wang, Y.; Li, M.; Yang, L. Element dependence of radiation-induced structural changes in metallic glasses. *J. Non-Cryst. Sol.* **2020**, *533*, 119933. [[CrossRef](#)]
80. Andrievskii, R.A. Radiation stability of nanomaterials. *Nanotechnol. Russia* **2011**, *6*, 357–369. [[CrossRef](#)]
81. Škorvánek, I.; Miglierini, M. The effects of short range order changes on hyperfine field distribution and Curie temperature of amorphous $\text{Fe}_{30}\text{Ni}_{36}\text{Cr}_{12}\text{Mo}_2\text{B}_{15}\text{Si}_5$. *J. Magn. Magn. Mater.* **1991**, *96*, 162–166. [[CrossRef](#)]
82. Xiong, F.; Li, M.-F.; Malomo, B.; Yang, L. Microstructural evolution in amorphous-nanocrystalline ZrCu alloy under neutron irradiation. *Acta Mater.* **2020**, *182*, 18–28. [[CrossRef](#)]
83. Pavúk, M.; Miglierini, M.; Vůjtek, M.; Mashlan, M.; Zbořil, R.; Jirásková, Y. AFM and Mössbauer spectrometry investigation of the nanocrystallization process in Fe-Mo-Cu-B rapidly quenched alloy. *J. Phys. Condens. Matter.* **2007**, *19*, 216219. [[CrossRef](#)]
84. Miglierini, M.; Šafářová, K. Magnetic features at the surfaces of nanocrystalline ribbons. *Acta Phys. Pol. A* **2010**, *118*, 840–842. [[CrossRef](#)]
85. Gupta, A.; Habibi, S.; Lal, S.; Principi, G. Mössbauer study of surface crystallization in metallic glasses. *Hyperfine Int.* **1990**, *55*, 967–972. [[CrossRef](#)]
86. Balúch, S.; Miglierini, M.; Gröne, R.; Sitek, J. Positron lifetime and Mössbauer study of $\text{Fe}_{80-x}\text{Ni}_x\text{B}_{20}$ metallic glasses. *Phys. Status Solidi. A Appl. Res.* **1989**, *113*, K143–K145. [[CrossRef](#)]